Article

Stacking Fault Nucleation in Films of Vertically Oriented Multiwall Carbon Nanotubes by Pyrolysis of Ferrocene and Dimethyl Ferrocene at a Low Vapor Flow Rate

Ayoub Taallah [1,2], Shanling Wang [3], Omololu Odunmbaku [4], Lin Zhang [1], Xilong Guo [1], Yixin Dai [1], Wenkang Li [1], Huanqing Ye [5], Hansong Wu [1], Jiaxin Song [1], Jian Guo [1], Jiqiu Wen [3], Yi He [3] and Filippo S. Boi [1,*]

[1] College of Physics, Sichuan University, Chengdu 610064, China; ayoub.taallah@univ-djelfa.dz (A.T.); 15298159228@163.com (L.Z.); gxl@stu.scu.edu.cn (X.G.); 2021322020022@stu.scu.edu.cn (Y.D.); 2022322020026@stu.ecnu.edu.cn (W.L.); wuhansong@stu.scu.edu.cn (H.W.); 2023326060017@stu.scu.edu.cn (J.S.); jianguo@scu.edu.cn (J.G.)

[2] Physico-Chemistry of Materials and Environment Laboratory, Physics Department, Ziane Achour University of Djelfa, Djelfa 17000, Algeria

[3] Analytical and Testing Centre, Sichuan University, Chengdu 610064, China; wangshanling@scu.edu.cn (S.W.); wenjiqiu@scu.edu.cn (J.W.); scu_heyi@126.com (Y.H.)

[4] MOE Key Laboratory of Low-Grade Energy Utilization Technologies and Systems, CQU-NUS Renewable Energy Materials & Devices Joint Laboratory, School of Energy and Power Engineering, Chongqing University, Chongqing 400044, China; o.odunmbaku@cqu.edu.cn

[5] Photon Science Institute, Department of Electrical and Electronic Engineering, University of Manchester, Manchester M19 1LL, UK; huanqing.ye@manchester.ac.uk

* Correspondence: f.boi@scu.edu.cn

Abstract: Recent observations of superconductivity in low-dimensional systems composed of twisted, untwisted, or rhombohedral graphene have attracted significant attention. One-dimensional moiré superlattices and flat bands have interestingly been identified in collapsed chiral carbon nanotubes (CNTs), opening up new avenues for the tunability of the electronic properties in these systems. The nucleation of hexagonal moiré superlattices and other types of stacking faults has also been demonstrated in partially collapsed and uncollapsed carbon nano-onions (CNOs). Here, we report a novel investigation on the dynamics of stacking fault nucleation within the multilayered lattices of micrometer-scale vertically oriented films of multiwall CNTs (MWCNTs), resulting from the pyrolysis of molecular precursors consisting of ferrocene or dimethyl ferrocene, at low vapor flow rates of ~5–20 mL/min. Interestingly, local nucleation of moiré-like superlattices (as stacking faults) was found when employing dimethyl ferrocene as the pyrolysis precursor. The morphological and structural properties of these systems were investigated with the aid of scanning and transmission electron microscopies, namely SEM, TEM, and HRTEM, as well as X-ray diffraction (XRD) and Raman point/mapping spectroscopy. Deconvolution analyses of the Raman spectra also demonstrated a local surface oxidation, possibly occurring on defect-rich interfaces, frequently identified within or in proximity of bamboo-like graphitic caps. By employing high-temperature Raman spectroscopy, we demonstrate a post-growth re-graphitization, which may also be visualized as an alternative way of depleting the oxygen content within the MWCNTs' interfaces through recrystallization.

Keywords: carbon nanotubes; stacking fault; moiré superlattice; ferrocene; dimethyl ferrocene

1. Introduction

Recent observations of superconductivity in systems composed of a few layers of graphene have attracted significant research interest in materials physics and nanotechnology [1–8]. Superconductive ordering has been shown to occur in ordinary bilayer graphene in the presence of suitably arranged electric and magnetic fields, indicating the possible presence of an exotic state for finite values of the magnetic field at B = 165 mT (applied

in the plane of the sample) [1,2]. Further, robust superconductivity has been reported to occur when a twist angle is applied between two or more graphene layers, leading to the appearance of hexagonal moiré superlattices and consequential emergence of van Hove singularities [3–8]. In these systems, insulating states and electron correlation phenomena have been reported to occur under specific values of the twist angle parameter [3–12]. In particular, superconductivity has been shown to occur for a specific value of the twist parameter of $\theta \sim 1.09°$ (magic angle) [3]. A dependence of the shape and position of the van Hove singularities on the value of the twist angle parameter has been interestingly demonstrated by Brihuega et al. [7], with significant additional effects arising in the presence of non-uniform periodicities of the moiré superlattices. The appearance of magnetic ordering and exotic magnetism within these systems has also been demonstrated for $\theta_{twist} \sim 1.2°$ [9] (orbital magnetism), $\theta_{twist} \sim 1.8°$ (exotic ferromagnetism) [10], $\theta_{twist} \sim 1.68°$ (orbital moiré magnetism) [11], and $\theta_{twist} < 0.1°$ (ferrimagnetic spin order) [12]. The stability of the identified superconductive phenomena has been reported to be strongly dependent on the quality of the twist angle parameter and layer adhesion [13,14]. The occurrence of stacking faults within moiré superlattices has also been shown to result in the disappearance of superconductive ordering [13,14] and/or other exotic phenomena, including variations in the shape, position, and sharpness of van Hove singularities [14]. Further, the number of graphene layers (comprised within the moiré superlattice [15]) has been shown to play a significant role in inducing shifts in the actual value of the magic angle. Interestingly, a theoretical model of alternating twist angles was reported by Khalaf et al. [15], predicting significant variation in the actual values of the θ_{twist} parameter for moiré superlattices derived from thick samples (i.e., samples consisting of multilayered graphene with alternating twist angles) [15]. Additionally, superconductive ordering has been reported at low temperature in samples consisting of consecutively stacked honeycomb layers of carbon atoms (ABC stacking) [16]. In this latter type of system, the atomic graphene sheets are arranged in such a way that every atom has a nearest neighbor from an adjacent layer either above or underneath. Multilayer graphene systems exhibiting a rhombohedral stacking order have interestingly been shown to also exhibit ferroelectric and multiferroic ordering [17,18]. A spontaneous energy gap has been interestingly shown to occur at sample thickness values below 4 nm, also in the absence of an applied electric field [19,20].

Stabilization of the rhombohedral stacking order has been further shown to occur in partially deformed [21,22] or stressed lattices [23].

Unusual superconductive-like phenomena have been also reported above 300 K [24–34], indicating a possible important role of the thickness and homogeneity of the moiré superlattice in the modification of the T_c parameters of these materials [34]. Together with these findings, superconductivity has been reported also in grafoil, within an unknown type of structural defect ($T_c \sim 14$ K [35]).

Recent works have also shown the possibility of stabilizing one-dimensional moiré superlattices in collapsed single-wall carbon nanotubes (CNTs) [36,37] and partially collapsed elongated carbon nano-onions (CNOs) [38]. These findings open up new avenues for the stabilization of van Hove singularities in films of nanoscale graphitic carbons.

Here, we report a novel investigation on the dynamics of stacking fault nucleation within the multilayered lattices of multiwall carbon nanotubes (MWCNTs), employing either ferrocene or dimethyl ferrocene as molecular precursors for the pyrolysis experiments. We demonstrate the nucleation of stacking faults consisting of moiré-like hexagonal superlattices by employing a chemical vapor deposition (CVD) approach, involving the sublimation and pyrolysis of dimethyl ferrocene at low vapor flow rates of ~10 mL/min. In particular, stacking faults were identified, when employing dimethyl ferrocene as the pyrolysis precursor, in proximity of bamboo-like caps, nucleated within the multilayered lattices of the local inner capillary regions of the MWCNTs, with a variable direction with respect to the tube axis. The morphological and structural properties of these systems were investigated by employing a large pool of experimental techniques, including scanning

and high-resolution transmission electron microscopy (SEM, TEM, and HRTEM), profile analyses, and X-ray diffraction (XRD) and Raman point and mapping spectroscopy.

2. Experiment

2.1. Synthesis

Free-standing films of aligned MWCNTs were produced by sublimation and pyrolysis of 100–250 mg of ferrocene or 200 mg of dimethyl ferrocene inside a quartz tube reactor of 1.5 m with a thickness of 2.5 mm, as shown in Figure 1. Ar flow rates (laminar flow) in the range of 5 mL/min to 20 mL/min were employed. The sublimation temperature was 450 °C, while the pyrolysis temperature was set to approximately ~990 °C. The duration of each growth experiment was approximately 8–10 min. The quartz tube reactor was cooled to room temperature by removing the furnace along a rail system with a quench (fast cooling) process. The employed fast cooling approach enabled the extraction of vertically aligned CNT (VA-CNT) films from the substrate surface through differential thermal contraction [39]. In the specific investigations reported in this work, we employed smooth Si/SiO_2 or tungsten grids as substrates for the CNT deposition.
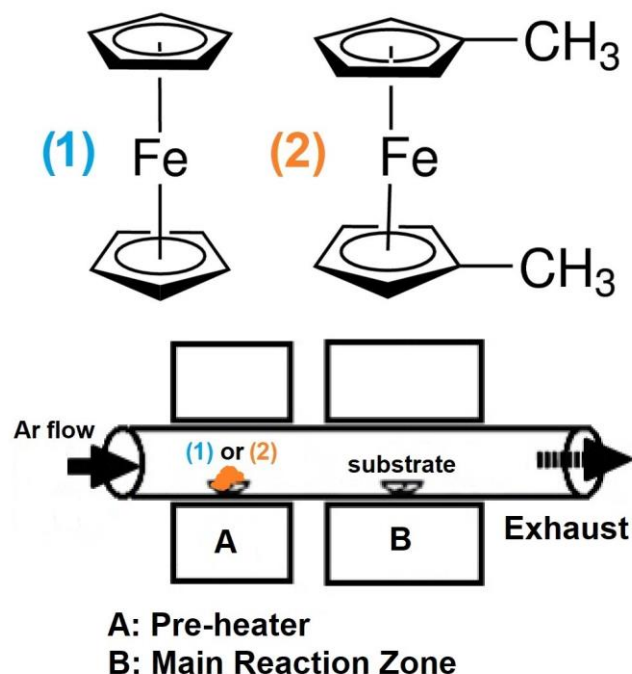

Figure 1. Schematic of the CVD system employed for the nucleation and growth of VA-MWCNTs, employing ferrocene or dimethyl ferrocene as the molecular precursor.

2.2. Characterization

Scanning electron microscopy (SEM) measurements were performed using a JSM-7500F (JEOL Ltd., Akishima, Tokyo, JAPAN) microscope at 5–20 kV. Transmission electron microscopy (TEM) and high-resolution TEM measurements were performed using a 200 kV American FEI Tecnai G2F20 microscope (FEI Company, Hillsboro, OR, USA) fitted with a field emission gun (FEG). Raman point and mapping measurements were performed with the Raman-AFM HR Evolution system (Horiba Jobin Yvon, Paris, France) at room temperature. The size of the selected mapping area was chosen as 40 × 40 μm. The numerical aperture of the objective lens was 0.7 mm at 100× magnification. High-temperature Raman spectroscopy measurements were performed using an Andor SR-500i (Oxford Instruments Technology (Shanghai) Co. Limited, Xuhui District, Shanghai, China) spectrometer with a wavelength of 532 nm and an acquisition time of approximately 100 s per sample. The measurements were conducted over a temperature range from 298 K to 673 K, with a beam exposure time of 22 min, at ambient pressure and in the presence of N_2 gas. Multiple XRD

acquisitions of the films were performed with a Philips Xpert pro MPD (PANalytical B.V., Almere, Flevoland, Netherlands) diffractometer (Cu K-α with λ = 0.154 nm) at room temperature and ambient pressure in the 2θ range from 10° to 70°. Rietveld refinement analyses were performed by employing General Structure Analysis System (GSAS) software (LANL, Los Alamos, NM, USA).

3. Results and Discussion

SEM investigations enabled the identification of the morphological properties of the as-grown free-standing vertically aligned MWCNTs. Figure S1A–E exhibit typical examples of the surface morphology of the as-grown free-standing films, resulting from the sublimation and pyrolysis of ferrocene and subsequential differential thermal contraction. As shown in Figure S1D, the films comprised vertically aligned close-packed nanotube structures. Interestingly, an unusual decoration of the CNT bundles with carbon nano-onion (CNO) particles was found, especially in experiments involving an Ar flow rate of 5 mL/min (see Figure S1E,F and cyan arrow in Figure S1E). These observations highlight the possible existence of intermediate growth modes (under the condition of a low vapor flow rate), with simultaneous nucleation and growth of both CNTs and CNOs and subsequential CNT decoration. Interestingly, comparable film morphologies could be identified when employing a metallic grid as the deposition substrate (in the presence of ferrocene as the precursor); this is observable in Figure S2A–F, with a progressively increasing magnification. As shown in Figure S2C–E, the films in this case were also found to exhibit a free-standing morphology, which derived from the differential thermal contraction process, after cooling. The high alignment of the CNTs was further confirmed by high-magnification analyses, as shown in Figure S2F, together with a significant amount of CNO decoration.

In an attempt to enhance the selectivity of the experiment towards the growth of aligned CNT bundles and deplete the quantities of CNO byproducts, extended investigations were performed using dimethyl ferrocene as a molecular precursor.

The micrographs in Figure 2A–F provide examples of the morphological characteristics of those VA-CNT films obtained when employing dimethyl ferrocene as the molecular precursor for the pyrolysis experiment. The high alignment of the CNTs is shown in Figure 2C–F. In particular, a depletion in the relative quantities of decorating CNOs was found when employing dimethyl ferrocene as a precursor. These observations were supported by extensive TEM and HRTEM characterization measurements and analyses, as shown in Figures 3A–F and 4–6. The TEM and HRTEM measurements presented in Figure 3A–F provide clear evidence of coexisting MWCNT and CNO morphologies within the films obtained when employing ferrocene as a molecular precursor. The observed coexistence of CNT and CNO growth modes is possibly attributable to the rapid sublimation of the ferrocene molecule, with consequential spontaneous nucleation of large quantities of catalyst particles by homogeneous nucleation within the reaction zone [40]. The presented results differ, however, from those reported by Elliott et al. [41] and Wu et al. [42], where the growth of CNO films resulted instead from experimental conditions involving a low carbon supply and lower sublimation temperatures of the precursor [41,42] and, therefore, from different nucleation dynamics of the carbon layers from the nanoparticles. Interestingly, subsequential lift-up growth effects have also been shown to occur in the CVD process [43].

Noticeably, significantly sharper interfaces could be found when employing dimethyl ferrocene (instead of ferrocene) as a molecular precursor, with a depletion in the amount of CNOs within the film.

The TEM and HRTEM analyses of such a morphological transition are presented in Figure 4 at low magnification and in Figure 5A–F at high magnification (high-resolution). When examining the micrographs presented in Figure 5A–F, the occurrence of graphitic caps with a variable orientation and close compartments is noticeable, which define a non-uniform inner CNT capillary. Note also the presence of strain and dislocation defects occurring within the thick graphitic layers of the MWCNT, as shown in Figure 5D–F. These strain-rich regions were also analyzed using DigitalMicrograph software through profile

investigations, with an appropriate integration width for the line profile, as presented in Figure 6A–D.
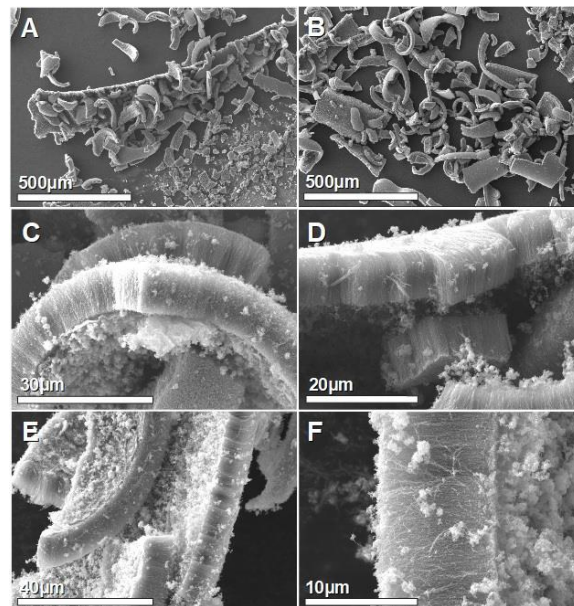

Figure 2. SEM micrographs (**A**–**F**) of typical flakes of free-standing films of MWCNTs obtained by pyrolysis of dimethyl ferrocene at a low Ar vapor flow rate of ~10 mL/min. In particular, the micrographs in (**C**–**E**) allow for a clear observation of the high degree of CNT alignment.
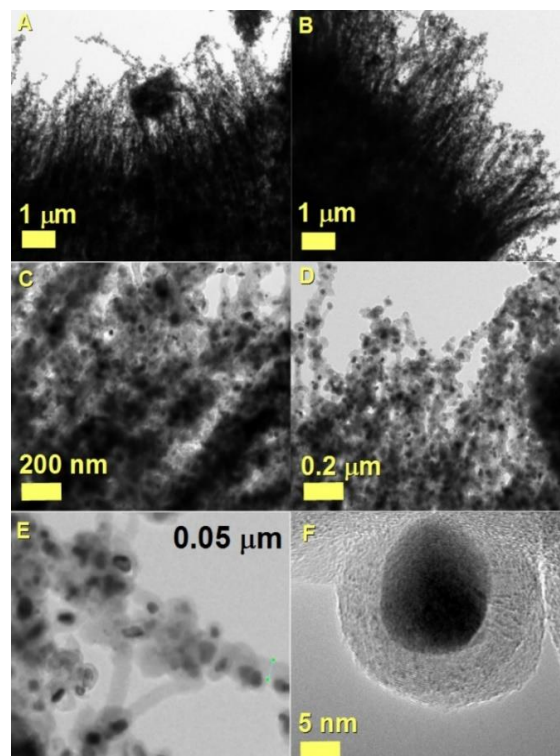

Figure 3. Transmission electron micrographs (**A**–**F**) showing, with an increasing level of detail, the cross-sectional morphology of films comprising vertically aligned MWCNTs decorated with filled CNOs. The TEM micrographs in (**E**,**F**) show the fine details of the CNOs decorating the MWCNT (scale bar in green corresponds to 0.05 μm). These films were obtained through the pyrolysis of ferrocene at very low vapor flow rates of ~5 mL/min.

In particular, Figure 6C,D provide an example of profile analyses applied to the thick graphitic structure of the MWCNT. These analyses highlight the presence of strain-rich interfaces. Further, when examining the micrograph in Figure 6B, a transition in the stacking order of the graphitic layers can be clearly found, implying the formation of stacking faults in proximity of partially nucleated graphitic caps with a variable orientation.

Detailed analyses of the observed stacking fault at high resolution are further shown in Figures 7 and 8. The profile investigations presented in Figure 8 highlight the nucleation of hexagonal domains, indicative of a local change of stacking order and/or partially twisted interfaces deriving from the variable orientation of the graphitic caps [44]. Interestingly, a super-periodicity ranging from ~0.4 to 0.6 nm could be identified by means of profile investigations (see Figure 8).
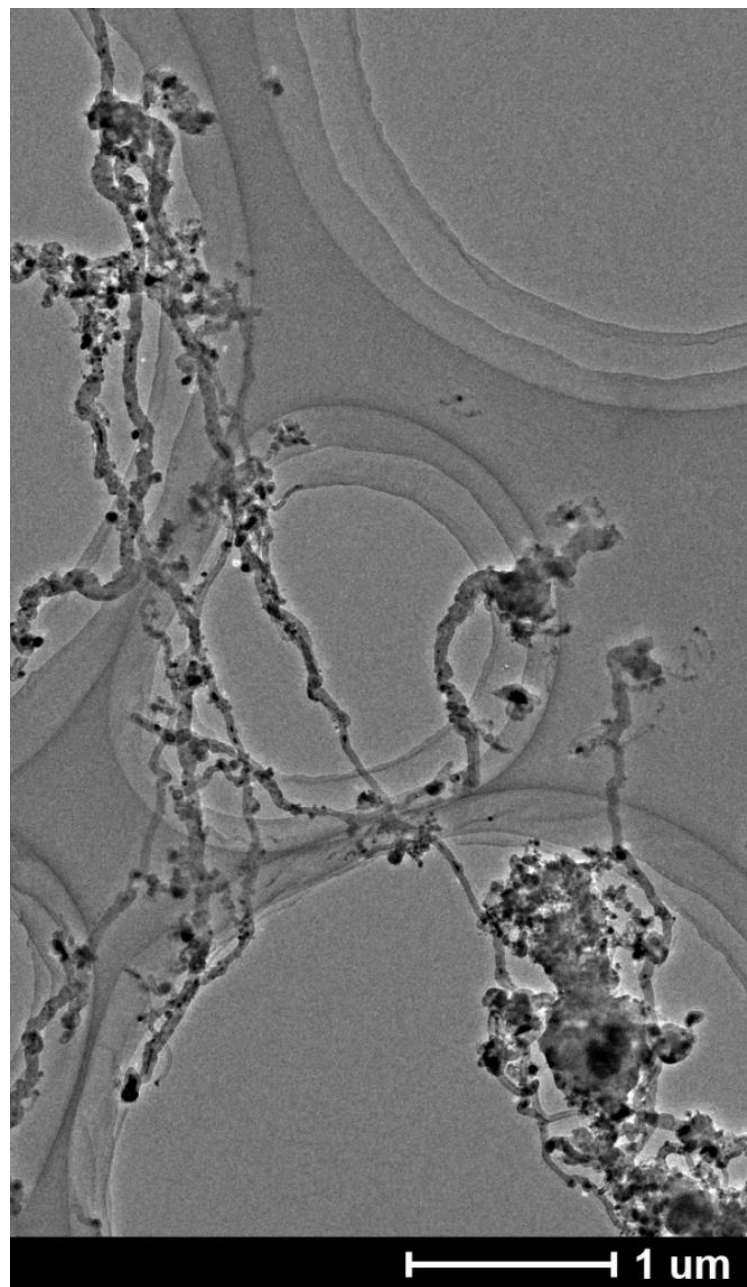

Figure 4. Low-magnification TEM micrograph of as-grown VA-MWCNTs obtained through the pyrolysis of dimethyl ferrocene.
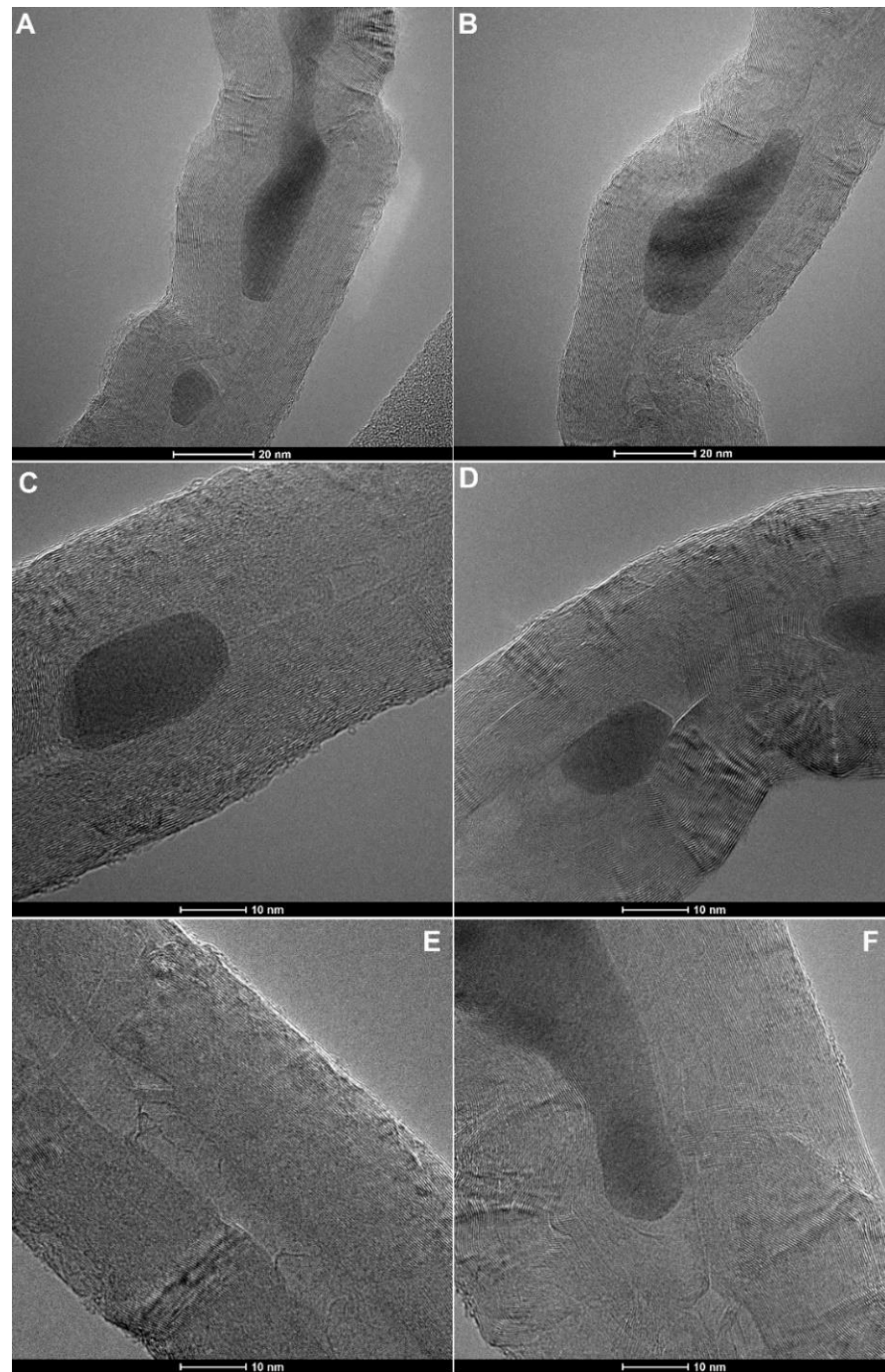
Figure 5. HRTEM micrographs (**A**–**F**) exhibiting the structural arrangement of the CNT walls. Note the presence of structural stress and dislocation-rich interfaces, as shown in (**D**–**F**). The formation of graphitic caps on both sides of the encapsulated particle indicates a bamboo-like growth mechanism with a variable orientation. The presence of stacking faults and moiré-like super-periodicities is visible in the micrograph presented in (**D**).

By applying the equation a/2D = sin (θ_{twist}/2) [44], where a is the basal lattice constant (~0.247 nm), D is the period of the moiré-like super-periodicity, and θ_{twist} is the rotational angle, a possible θ_{twist} ~ 33–35° could be identified within the moiré-like stacking fault area. Interestingly, the period of the stacking fault moiré-like superlattice is analogous with that of ~0.5 nm previously reported in scanning tunneling microscopy (STM) investigations of highly oriented pyrolytic graphite (HOPG), which exhibited weak van Hove singularities in the local density of states (LDOS) acquisitions [44]. In an attempt to further evaluate

the origin of the observed structural transitions occurring within the inner capillary of the MWCNTs, an additional investigation was conducted on the catalyst particles by means of XRD and Rietveld refinements. As shown in Figure 9, these investigations revealed a large relative abundance of Fe_3C (74.8%) in coexistence with α-Fe (18.6%) and γ-Fe (6.6%) phases (see also ESI Figure S3). Interestingly, a comparable structural arrangement of the catalyst has been recently shown by Wu et al. [38] in partially collapsed CNOs.
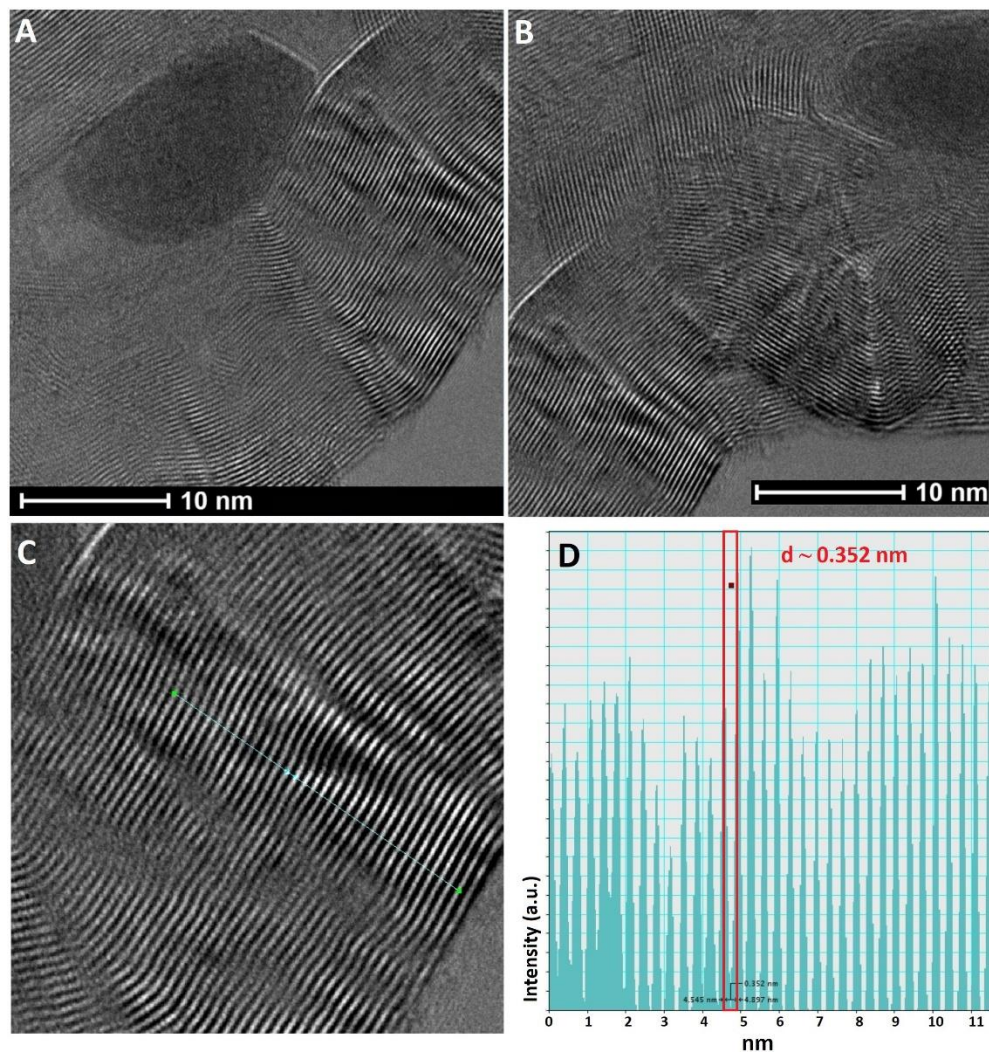

Figure 6. HRTEM (**A**–**C**) and profile analyses (**D**) revealing the presence of a transition in the stacking order of the CNT walls in proximity of partially nucleated graphite caps (see (**B**)).

Additional structural characterization of the films was then conducted using Raman point and mapping spectroscopy. As shown in Figure 10A–D, the map analyses revealed a significant local variation in the amplitude of the D and G band components, with the appearance of D′ band features indicating an enhancement in the relative abundance of defect-rich carbon within certain regions of the CNT film. In particular, Figure 10C,D highlight a significant contribution arising from the D′ component. Considering the vertical alignment of the CNTs and the HRTEM analyses presented above, a higher density of structural defects is expectable in proximity of the CNT capping regions. The typical point spectra acquisitions presented in Figure 10E,F highlight the local variation of the D band intensity within the defect-rich regions of the film. In particular, the significant enhancement of the intensity of the D band, together with the sharp collapse of the G band intensity in E, may indicate the presence of local structural transitions, possibly involving the presence of partial collapse of the CNT structure.
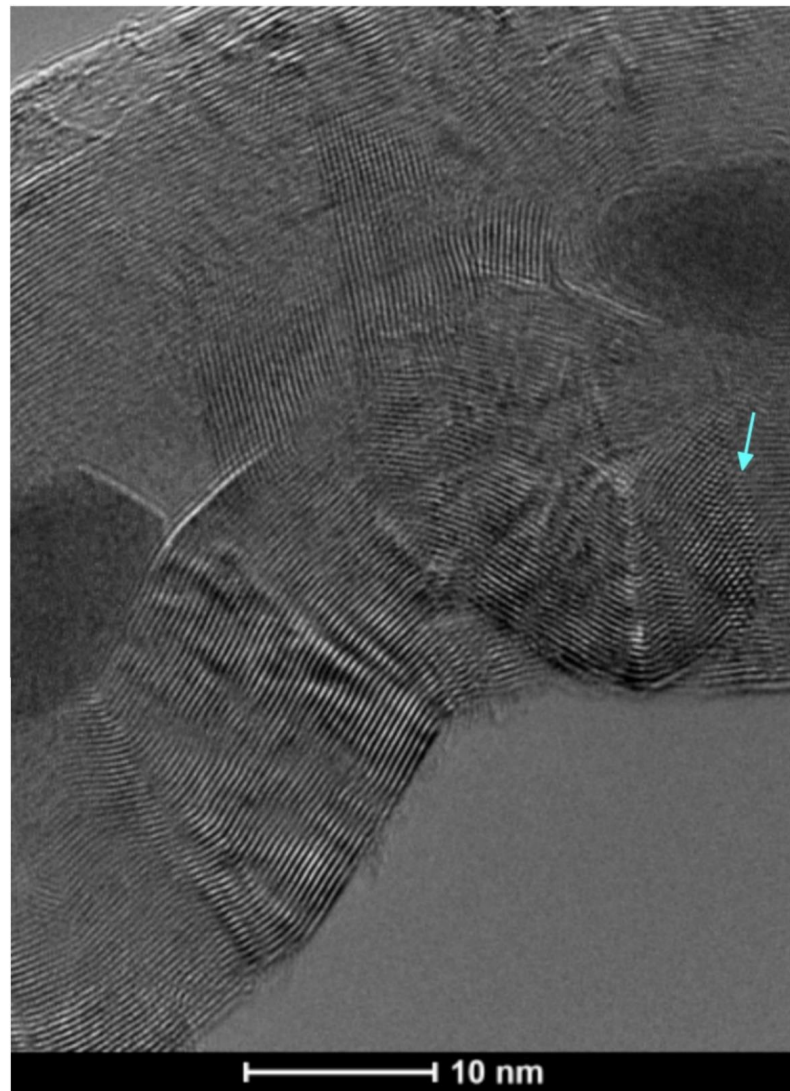
Figure 7. HRTEM micrograph revealing, with high detail, the nucleation of moiré-like stacking faults within the walls of the CNT, as a result of a variation in the orientation of the multilayered lattice. The nucleation of this type of stacking fault appears to be linked to the formation of graphitic bamboo-like caps with a variable orientation (see cyan arrow).

Further analyses of the as-grown films were then conducted by employing high-temperature Raman spectroscopy. Continuous laser beam exposure measurements were obtained at T ~ 673 K following the conditions reported by Taallah et al. for carbon onion samples [45]. Interestingly, a decrease in the amplitude of the D and G bands can be found in Figures 11 and 12 with the increase in the laser beam exposure time (particularly after 1 min of exposure). The observed changes in the amplitudes of the D and G bands appear to possibly indicate the presence of a recrystallization (re-graphitization) process which enhances the crystallinity of the whole hybrid system, with a consequential decrease in the intensity of those bands associated with interface oxidation [38,46]. Detailed deconvolution analyses of the Raman spectra are shown in Figure 11A,B. Note the variation in the intensity of the defect-induced splitting of the D band component, which is indicative of (1) partial recrystallization of amorphous CNT lattices and (2) progressive depletion of C-O bonding as a consequence of the film recrystallization. The evolution of the 2D band as a function of the laser exposure time is presented in the plot of Figure 13. Interestingly, an approximately linear increase in the 2D band area with increasing laser exposure time is demonstrated, confirming the existence of a partial re-graphitization.
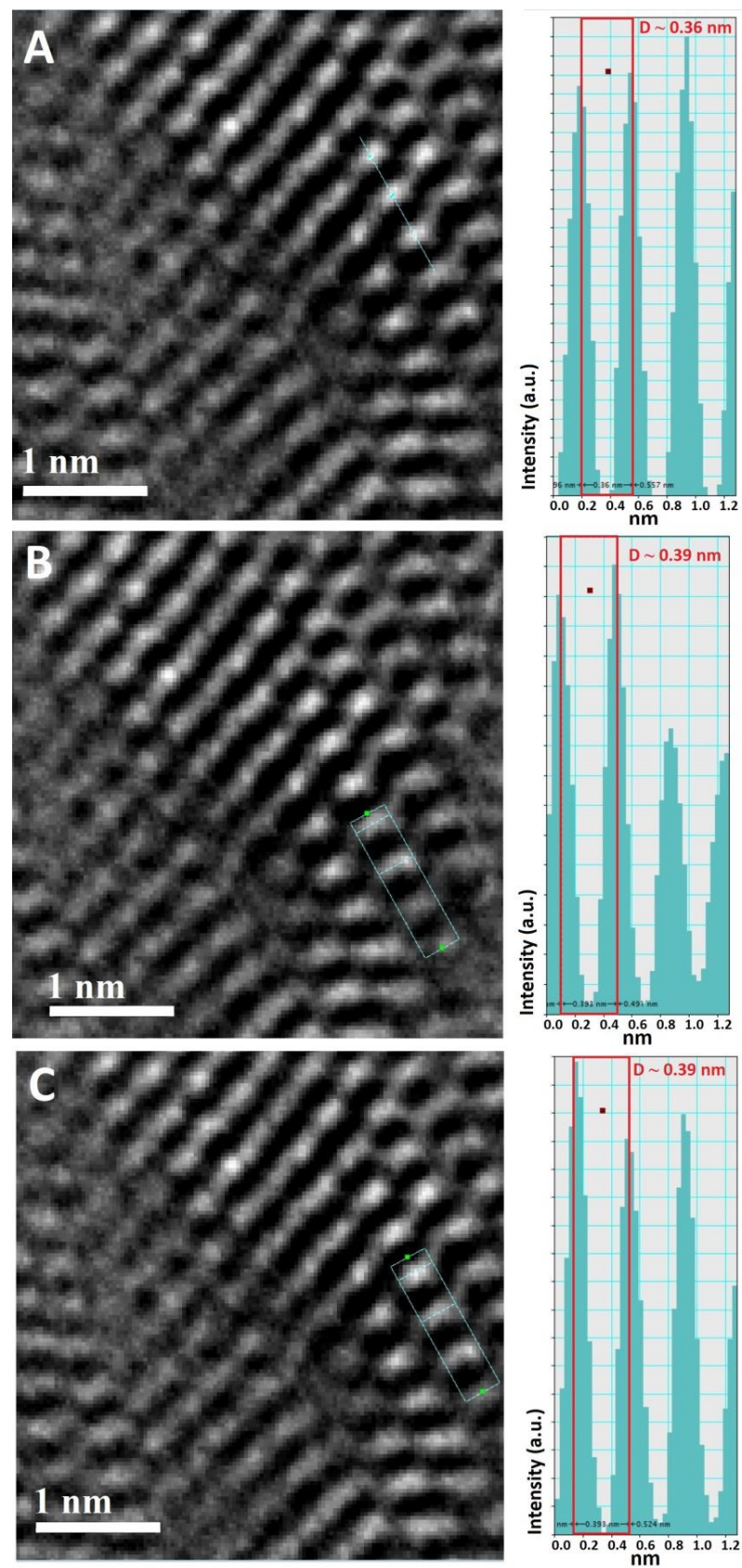
Figure 8. HRTEM micrograph of the stacking fault shown in Figure 7 (cyan arrow) and profile analyses (**A**–**C**) performed with the aid of DigitalMicrograph software, revealing examples of super-periodicities D ranging from ~0.4 nm to ~0.6 nm.
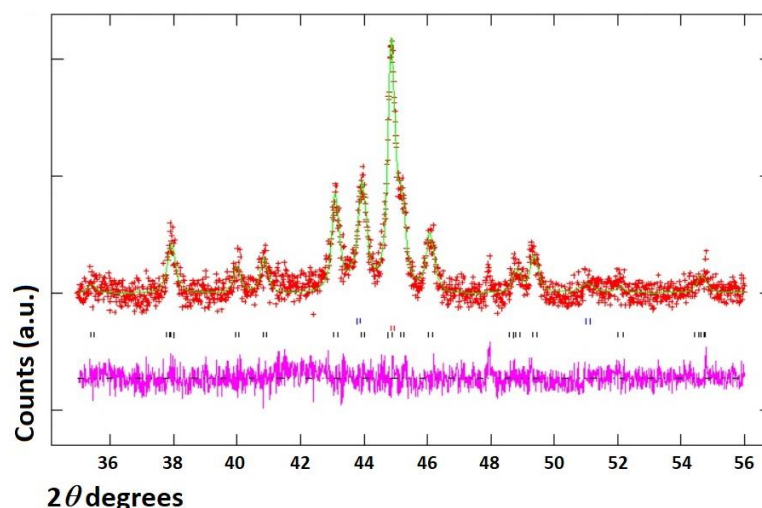
Figure 9. Typical XRD diffractogram (red line) and Rietveld refinement (green line) of the free-standing aligned MWCNT films, revealing the following phase abundances: 74.8% Fe_3C, 18.6% α-Fe, and 6.6% γ-Fe. The magenta line corresponds to the difference between the XRD diffractogram (experimental data) and the Rietveld model (theoretical data). The extracted R_p value was 0.0278. The following database cards were employed for the refinements: COD 1008725 (Fe_3C with space group Pnma), COD 1100108 (α-Fe with space group Im-3m), and COD 1534888 (γ-Fe with space group Fm-3m). See ESI Figure S3 for details on extracted unit cell parameters.
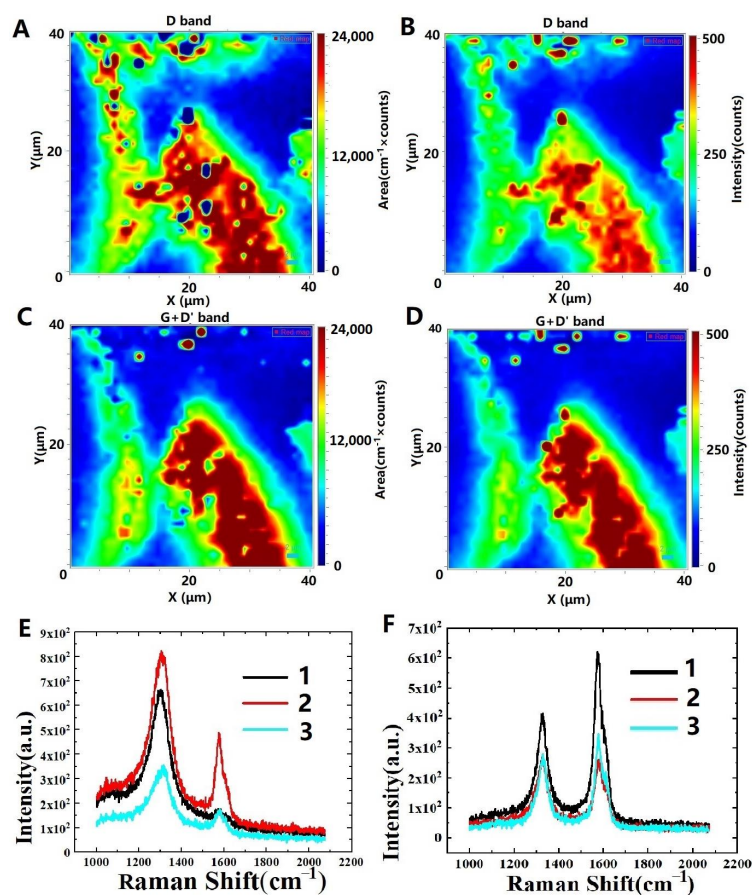

Figure 10. Typical examples of Raman spectroscopy point/map analyses of the VA-MWCNT. The map analyses in (**A**–**D**) and the point analyses in (**E**,**F**) highlight a significant local variation in the amplitude of the D and G band components, with the appearance of D′ band features indicative of an enhancement in the relative abundance of defect-rich carbon within certain regions of the film.

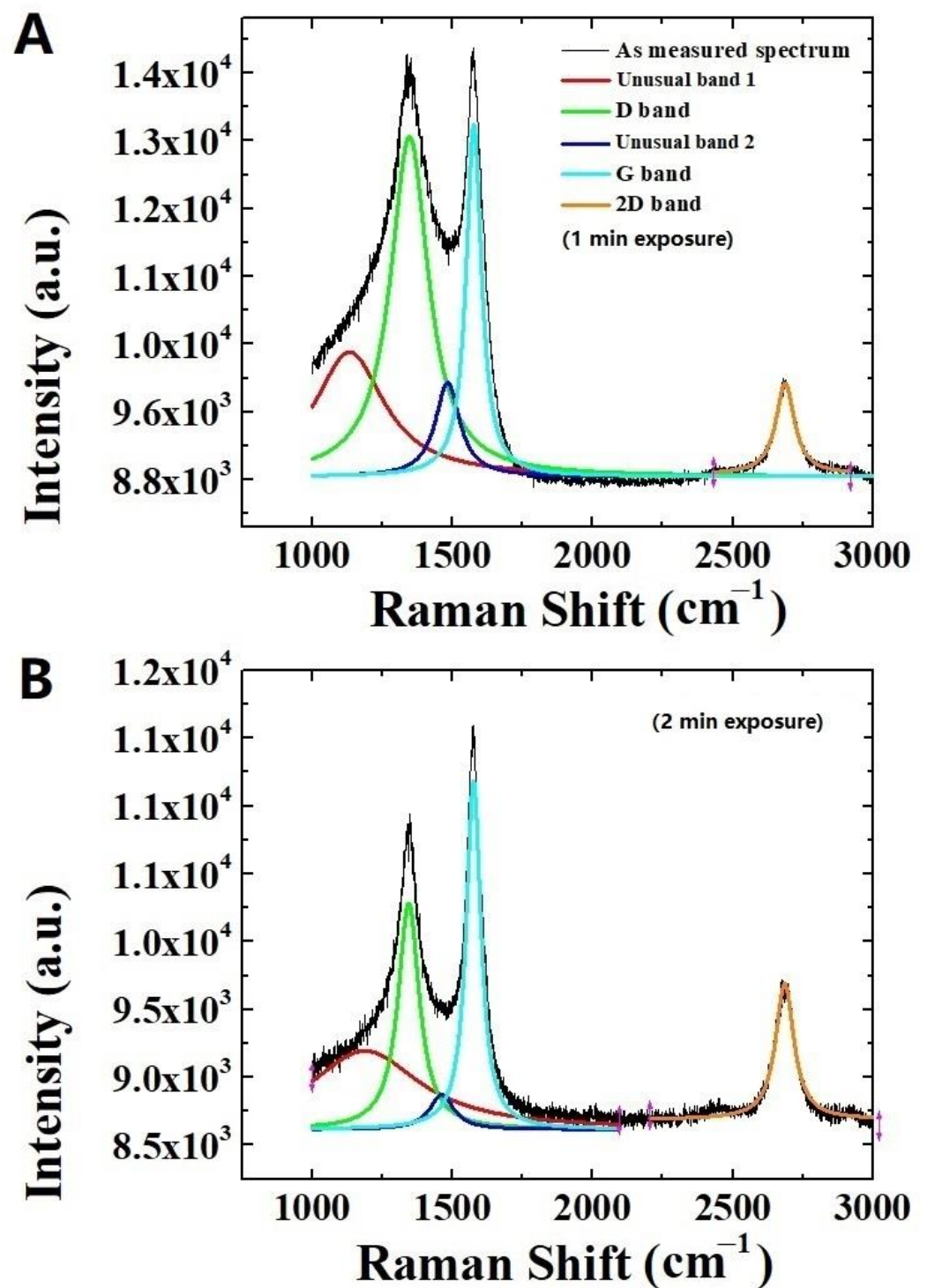**Figure 11.** In (**A**,**B**) deconvolution analyses of the Raman spectra collected at T ~ 673 K after 1 min (**A**) and 2 min (**B**) of laser exposure, respectively, evidencing the presence of an enhanced 2D band in (**B**), deriving from a re-graphitization process.

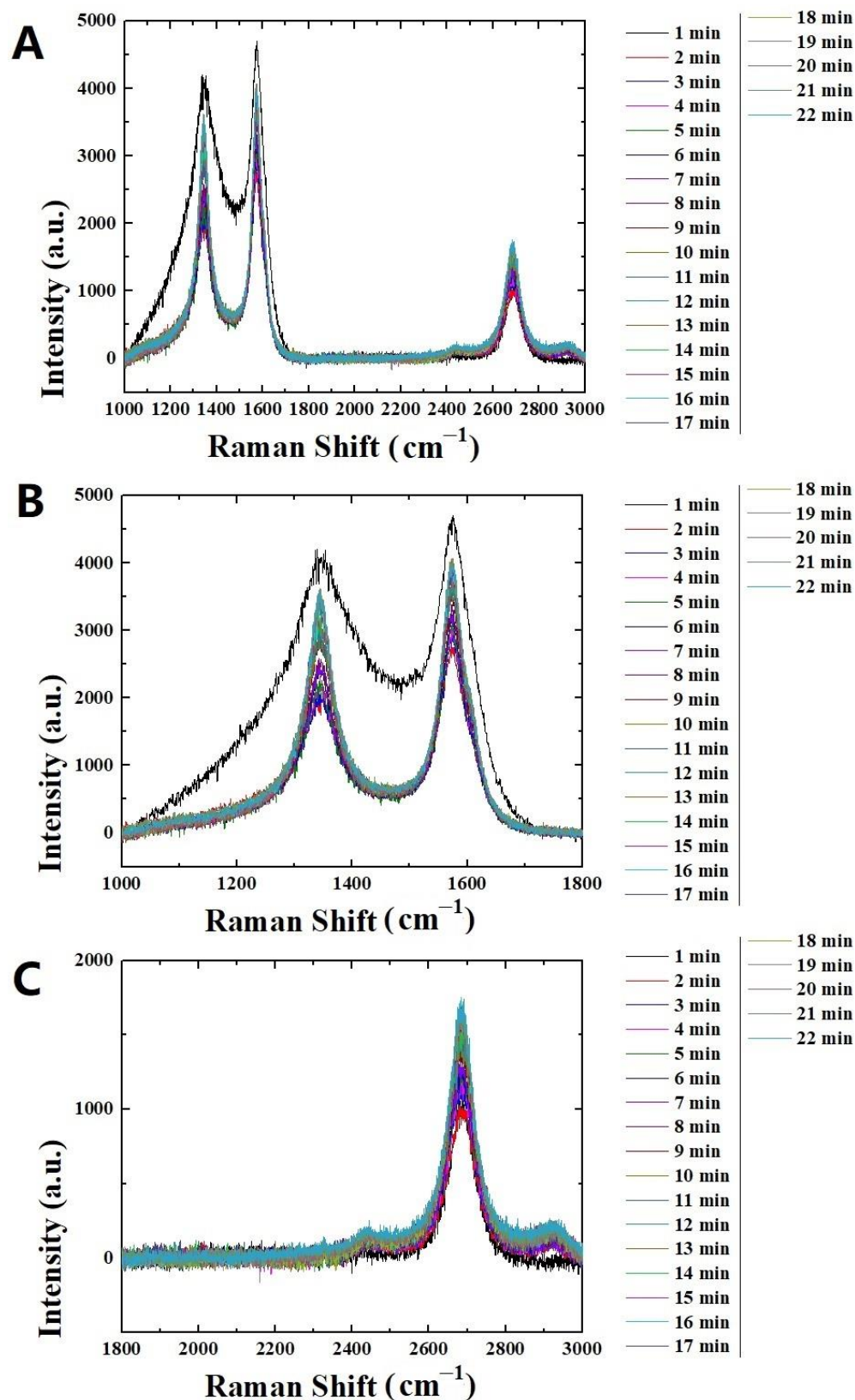**Figure 12.** High-temperature Raman spectroscopy measurement showing the variation in the intensities of D, G, and 2D bands as a function of laser beam exposure time for a constant temperature (T ~ 673 K under N_2 flow). This is shown in a large frequency range in (**A**), from 1000 to 3000 cm^{-1} and shorter frequency range in (**B**,**C**) from 1000 to 1800 and from 1800 to 3000 cm^{-1} respectively.
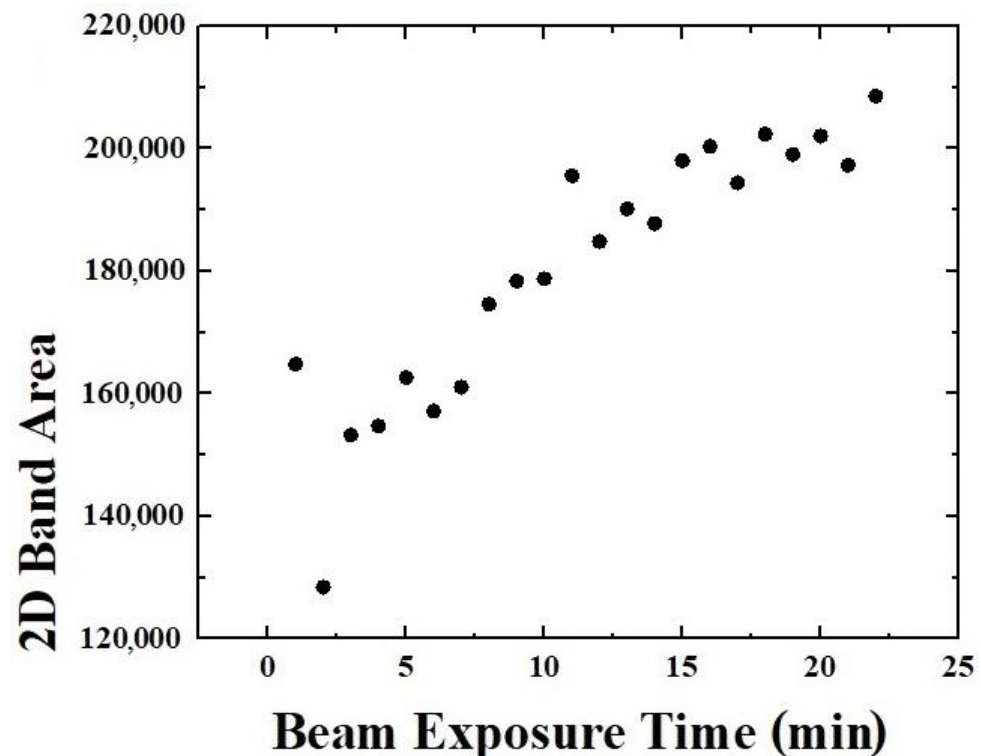
Figure 13. Evolution of the amplitude of the 2D band as a function of the laser beam exposure time, at T ~ 673 K.

4. Conclusions

In conclusion, we have reported the nucleation of moiré-like stacking faults within multilayered lattices of multiwall carbon nanotubes (MWCNTs) fabricated through the pyrolysis of dimethyl ferrocene, at low vapor flow rates of ~5–20 mL/min. The morphological and structural properties of the as-grown samples were investigated by employing a large pool of techniques, namely SEM, TEM, HRTEM, profile analyses, XRD, and Raman point and mapping spectroscopy. Additionally, the results obtained by employing high-temperature Raman spectroscopy revealed a post-growth re-graphitization effect. This approach may be visualized as a possible alternative experimental route for the recrystallization of MWCNT interfaces. The presented datasets may open up new avenues for the nucleation of stacking faults and, eventually, low-dimensional moiré superlattices in these systems. The collapse of hexagonal moiré superlattices and 1D defect strings have also been recently identified as technological targets allowing for the possible stabilization of Luttinger liquid states [47–49] and/or superconductivity in 1D systems [50,51].

Supplementary Materials: The following supporting information can be downloaded at: https://www.mdpi.com/article/10.3390/c10040091/s1, Figure S1: SEM micrographs A-F showing (with an increasing level of detail) the surface morphology of the as grown film (A–C), comprising of vertically aligned CNTs decorated with filled CNOs (at vapour flow rates of 5 mL/min). The high alignment of the CNTs in the film is visible in D, while the CNO decoration is presented in E,F. The cyan arrow in E indicates an example of decorated CNT (see experimental section for further details on the method of production); Figure S2: Typical examples of SEM micrographs (A–F) exhibiting the morphological aspects of typical VA-MWCNT films obtained by pyrolysis of ferrocene at low vapour flow rate, when employing a metallic grid as deposition substrate. Note the presence of free-standing VACNT morphologies which derive from the differential thermal contraction process. In E,F the morphological aspects of the VACNTs evidence a high alignment of the CNT-bundles and decoration with CNO-particles; Figure S3: Additional example of Rietveld refinement analysis of a typical XRD diffractogram of the film. The green line represents the theoretical fit to the XRD data (red crosses). The following unit cell parameters could be extracted, namely Fe_3C (Pnma) a = 0.506 nm,

b = 0.672 nm, c = 0.451 nm, α-Fe (Im-3m) a = b = c = 0.287 nm and γ-Fe (Fm-3m) a = b = c = 0.357 nm; Figure S4: Statistical distribution of the inner and outer CNO diameters, for samples produced at 5 mL/min, by pyrolysis of ferrocene.

Author Contributions: Conceptualization, A.T., S.W., O.O., L.Z., X.G., Y.D., W.L., H.Y., H.W., J.S., J.G., J.W., Y.H. and F.S.B.; methodology, A.T., S.W., O.O., L.Z., X.G., Y.D., W.L., H.W., Y.H. and F.S.B.; software, A.T., S.W., O.O., L.Z., X.G., Y.D., W.L., H.Y., H.W., J.S. and F.S.B.; validation, A.T., S.W., O.O. and F.S.B.; formal analysis, A.T., S.W., O.O., L.Z., X.G., Y.D., W.L., H.Y., H.W., J.S., J.G., J.W., Y.H. and F.S.B.; investigation, A.T., S.W., O.O., L.Z., X.G., Y.D., W.L., H.Y., H.W., J.S., J.G., J.W., Y.H. and F.S.B.; resources, S.W. and F.S.B.; data curation, A.T.; writing—original draft preparation, F.S.B.; writing—review and editing, A.T., O.O., H.Y., H.W., J.G. and F.S.B.; visualization, A.T., S.W., O.O., L.Z., X.G., Y.D., W.L., H.Y., H.W., J.S., J.G., J.W., Y.H. and F.S.B.; supervision, F.S.B.; project administration, F.S.B.; funding acquisition, F.S.B. All authors have read and agreed to the published version of the manuscript.

Funding: This research was funded by Sichuan University and the Sichuan University Research Leader fund.

Data Availability Statement: Original datasets may be made available on request.

Acknowledgments: Filippo Boi is grateful for the financial support from Sichuan University and the Sichuan University Research Leader fund. We thank Shanling Wang of the Analytical and Testing Center of Sichuan University for the help with HRTEM.

Conflicts of Interest: The authors declare no conflict of interest.

References

1. Zhou, H.; Holleis, L.; Saito, Y.; Cohen, L.; Huynh, W.; Patterson, C.L.; Yang, F.; Taniguchi, T.; Watanabe, K.; Young, A.F. Isospin magnetism and spin-polarized superconductivity in Bernal bilayer graphene. *Science* **2022**, *375*, 774–778. [CrossRef] [PubMed]
2. Heikkilä, T.T. Surprising superconductivity of graphene. *Science* **2022**, *375*, 719–720. [CrossRef] [PubMed]
3. Cao, Y.; Fatemi, V.; Fang, S.; Watanabe, K.; Taniguchi, T.; Kaxiras, E.; Jarillo-Herrero, P. Unconventional superconductivity in magic-angle graphene superlattices. *Nature* **2018**, *556*, 43–50. [CrossRef] [PubMed]
4. Park, J.M.; Cao, Y.; Watanabe, K.; Taniguchi, T.; Jarillo-Herrero, P. Tunable strongly coupled superconductivity in magic-angle twisted trilayer graphene. *Nature* **2021**, *590*, 249–255. [CrossRef]
5. Uri, A.; Grover, S.; Cao, Y.; Crosse, J.A.; Bagani, K.; Rodan-Legrain, D.; Myasoedov, Y.; Watanabe, K.; Taniguchi, T.; Moon, P.; et al. Mapping the twist-angle disorder and Landau levels in magic-angle graphene. *Nature* **2020**, *581*, 47–52. [CrossRef]
6. Li, G.; Luican, A.; Lopes dos Santos, J.M.B.; Castro Neto, A.H.; Reina, A.; Kong, J.; Andrei, E.Y. Observation of Van Hove singularities in twisted graphene layers. *Nat. Phys.* **2010**, *6*, 109–113. [CrossRef]
7. Brihuega, I.; Mallet, P.; González-Herrero, H.; de Laissardière, G.T.; Ugeda, M.M.; Magaud, L.; Gómez-Rodríguez, J.M.; Ynduráin, F.; Veuillen, J.-Y. Unraveling the Intrinsic and robust nature of van hove singularities in twisted bilayer graphene by scanning tunneling microscopy and theoretical analysis. *Phys. Rev. Lett.* **2012**, *109*, 196802. [CrossRef]
8. Yankowitz, M.; Chen, S.; Polshyn, H.; Zhang, Y.; Watanabe, K.; Taniguchi, T.; Graf, D.; Young, A.F.; Dean, C.R. Tuning superconductivity in twisted bilayer graphene. *Science* **2019**, *363*, 1059. [CrossRef]
9. Sharpe, A.L.; Fox, E.J.; Barnard, A.W.; Finney, J.; Watanabe, K.; Taniguchi, T.; Kastner, M.A.; Goldhaber-Gordon, D. Emergent ferromagnetism near three-quarters filling in twisted bilayer graphene. *Science* **2019**, *365*, 605–608. [CrossRef]
10. Seo, K.; Kotov, V.N.; Uchoa, B. Ferromagnetic Mott state in twisted graphene bilayers at the magic angle. *Phys. Rev. Lett.* **2019**, *122*, 246402. [CrossRef]
11. Li, S.-Y.; Zhang, Y.; Ren, Y.-N.; Liu, J.; Dai, X.; He, L. Experimental evidence for orbital magnetic moments generated by moiré-scale current loops in twisted bilayer graphene. *Phys. Rev. B* **2020**, *102*, 121406. [CrossRef]
12. Kerelsky, A.; Rubio-Verdú, C.; Xian, L.; Kennes, D.M.; Halbertal, D.; Finney, N.; Song, L.; Turkel, S.; Wang, L.; Watanabe, K.; et al. Moiréless correlations in ABCA graphene. *Proc. Natl. Acad. Sci. USA* **2021**, *118*, e2017366118. [CrossRef] [PubMed]
13. Wilson, J.H.; Fu, Y.; Sarma, S.D.; Pixley, J.H. Disorder in twisted bilayer graphene. *Phys. Rev. Res.* **2020**, *2*, 023325. [CrossRef]
14. Turkel, S.; Swann, J.; Zhu, Z.; Christos, M.; Watanabe, K.; Taniguchi, T.; Sachdev, S.; Scheurer, M.S.; Kaxiras, E.; Dean, C.R.; et al. Orderly disorder in magic-angle twisted trilayer graphene. *Science* **2022**, *376*, 193–199. [CrossRef] [PubMed]
15. Khalaf, E.; Kruchkov, A.J.; Tarnopolsky, G.; Vishwanath, A. Magic angle hierarchy in twisted graphene multilayers. *Phys. Rev. B* **2019**, *100*, 085109. [CrossRef]
16. Zhou, H.; Xie, T.; Taniguchi, T.; Watanabe, K.; Young, A.F. Superconductivity in rhombohedral trilayer graphene. *Nature* **2021**, *598*, 434–438. [CrossRef]
17. Han, T.; Lu, Z.; Scuri, G.; Sung, J.; Wang, J.; Han, T.; Watanabe, K.; Taniguchi, T.; Fu, L.; Park, H.; et al. Orbital multiferroicity in pentalayer rhombohedral graphene. *Nature* **2023**, *623*, 41–47. [CrossRef]

18. Winterer, F.; Geisenhof, F.R.; Fernandez, N.; Seiler, A.M.; Zhang, F.; Weitz, R.T. Ferroelectric and spontaneous quantum Hall states in intrinsic rhombohedral trilayer graphene. *Nat. Phys.* **2024**, *20*, 422–427. [CrossRef]

19. Yang, Y.; Zou, Y.-C.; Woods, C.R.; Shi, Y.; Yin, J.; Xu, S.; Ozdemir, S.; Taniguchi, T.; Watanabe, K.; Geim, A.K.; et al. Stacking Order in Graphite Films Controlled by van der Waals Technology. *Nano Lett.* **2019**, *19*, 8526–8532. [CrossRef]

20. Shi, Y.; Xu, S.; Yang, Y.; Slizovskiy, S.; Morozov, S.V.; Son, S.-K.; Ozdemir, S.; Mullan, C.; Barrier, J.; Yin, J.; et al. Electronic phase separation in multilayer rhombohedral graphite. *Nature* **2020**, *584*, 210–214. [CrossRef]

21. Freise, E.J.; Kelly, A. The deformation of graphite crystals and the production of the rhombohedral form. *Philos. Mag.* **1963**, *93*, 1519–1533. [CrossRef]

22. Boi, F.S.; Lee, C.-Y.; Wang, S.; Wu, H.; Li, L.; Zhang, L.; Song, J.; Dai, Y.; Taallah, A.; Odunmbaku, O.; et al. Rhombohedral stacking-faults in exfoliated highly oriented pyrolytic graphite. *Carbon Trends* **2024**, *15*, 100345. [CrossRef]

23. Nery, J.P.; Calandra, M.; Mauri, F. Long-Range Rhombohedral-Stacked Graphene through Shear. *Nano Lett.* **2020**, *20*, 5017–5023. [CrossRef] [PubMed]

24. Esquinazi, P.; Heikkilä, T.T.; Lysogoskiy, Y.V.; Tayurskii, D.A.; Volovik, G.E. On the superconductivity of graphite interfaces. *JETP Lett.* **2014**, *100*, 336–339. [CrossRef]

25. Ariskina, R.; Stiller, M.; Precker, C.E.; Böhlmann, W.; Esquinazi, P.D. On the Localization of Persistent Currents Due to Trapped Magnetic Flux at the Stacking Faults of Graphite at Room Temperature. *Materials* **2022**, *15*, 3422. [CrossRef]

26. Ballestar, A.; Barzola-Quiquia, J.; Scheike, T.; Esquinazi, P. Josephson-coupled superconducting regions embedded at the interfaces of highly oriented pyrolytic graphite. *New J. Phys.* **2013**, *15*, 023024. [CrossRef]

27. Esquinazi, P.D. Ordered Defects: A Roadmap towards room temperature Superconductivity and Magnetic Order. *arXiv* **2019**, arXiv:1902.07489.

28. Precker, C.E.; Esquinazi, P.D.; Champi, A.; Barzola-Quiquia, J.; Zoraghi, M.; Muiños-Landin, S.; Setzer, A.; Böhlmann, W.; Spemann, D.; Meijer, J.; et al. Identification of a possible superconducting transition above room temperature in natural graphite crystals. *New J. Phys.* **2016**, *18*, 113041. [CrossRef]

29. Precker, C.E.; Barzola-Quiquia, J.; Chan, M.K.; Jaime, M.; Esquinazi, P.D. High-field and high-temperature magnetoresistance reveals the superconducting behavior of the stacking faults in multilayer graphene. *Carbon* **2023**, *203*, 462–468. [CrossRef]

30. Kopnin, N.B.; Heikkilä, T.T.; Volovik, G.E. High-temperature surface superconductivity in topological flat-band systems. *Phys. Rev. B* **2011**, *83*, 220503. [CrossRef]

31. Kopnin, N.B.; Ijäs, M.; Harju, A.; Heikkilä, T.T. High-temperature surface superconductivity in rhombohedral graphite. *Phys. Rev. B* **2013**, *87*, 140503. [CrossRef]

32. Kopnin, N.B.; Heikkilä, T.T. Surface Superconductivity in Rhombohedral Graphite. In *Carbon-Based Superconductors: Towards High-Tc Superconductivity*; Haruyama, J., Jenny, S., Eds.; Taylor & Francis Group: London, UK, 2014; Chapter 9; pp. 231–263.

33. Rousset-Zenou, R.; Layek, S.; Monteverde, M.; Gay, F.; Dufeu, D.; Núñez-Regueiro, M. Hidden Granular Superconductivity Above 500K in off-the-shelf graphite materials. *arXiv*, 2022; arXiv:2207.09149.

34. Layek, S.; Monteverde, M.; Garbarino, G.; Méasson, M.-A.; Sulpice, A.; Bendiab, N.; Rodière, P.; Cazali, R.; Hadj-Azzem, A.; Nassif, V.; et al. Possible high temperature superconducting transitions in disordered graphite obtained from room temperature deintercalated KC8. *Carbon* **2023**, *201*, 667–678. [CrossRef]

35. Arnold, F.; Nyéki, J.; Saunders, J. Superconducting Sweet-Spot in Microcrystalline Graphite Revealed by Point-Contact Spectroscopy. *Jetp Lett.* **2018**, *107*, 577–578. [CrossRef]

36. Arroyo-Gascón, O.; Fernández-Perea, R.; Suarez Morell, E.; Cabrillo, C.; Chico, L. One-Dimensional Moiré Superlattices and Flat Bands in Collapsed Chiral Carbon Nanotubes. *Nano Lett.* **2020**, *20*, 7588–7593. [CrossRef]

37. Zhou, X.; Chen, Y.; Chen, J.; Hu, C.; Lyu, B.; Xu, K.; Lou, S.; Shen, P.; Ma, S.; Wu, Z.; et al. Pressure-induced flat bands in one-dimensional moiré superlattices of collapsed chiral carbon nanotubes. *Phys. Rev. B* **2024**, *109*, 045105. [CrossRef]

38. Wu, H.; Wang, S.; Gu, A.; Boi, F.S. Stacking-faults and moiré superlattice nucleation within the graphitic layers of partially-collapsed carbon nano-onions filled with γ-Fe: The role of indium isopropoxide as growth-promoter. *New J. Chem.* **2024**, *48*, 14521–14526. [CrossRef]

39. Boi, F.S.; Medranda, D.; Ivaturi, S.; Wang, J.; Guo, J.; Lan, M.; Wen, J.; Wang, S.; He, Y.; Mountjoy, G.; et al. Peeling off effects in vertically aligned Fe3C filled carbon nanotubes films grown by pyrolysis of ferrocene. *J. Appl. Phys.* **2017**, *121*, 244302. [CrossRef]

40. Jones, A.C.; Hitchman, M.L. (Eds.) *Chemical Vapour Deposition: Precursors, Processes, and Applications*; RSC Publishing: London, UK, 2008.

41. Elliott, B.R.; Host, J.J.; Dravida, V.P.; Teng, M.H.; Hwang, J.-H. A descriptive model linking possible formation mechanisms for graphite-encapsulated nanocrystals to processing parameters. *J. Mater. Res.* **1997**, *12*, 3328–3344. [CrossRef]

42. Wu, H.; Song, J.; He, Y.; Wang, S.; Lei, L.; Wen, J.; Gu, A.; Zhang, H.; Boi, F.S. Magnetic coupling in cm-scale buckypapers of self-organized Fe/Fe3C-filled carbon nano-onions: A controlled chemical vapor deposition approach. *Diam. Relat. Mater.* **2022**, *130*, 109503. [CrossRef]

43. Pinault, M.; Pichot, V.; Khodja, H.; Launois, P.; Reynaud, C.; Mayne-L'Hermite, M. Evidence of sequential lift in growth of aligned multiwalled carbon nanotube multilayers. *Nano Lett.* **2005**, *5*, 2394. [CrossRef]

44. Boi, F.S.; Taallah, A.; Gao, S.; Wang, S.; Corrias, A. Scanning tunneling microscopy identification of van Hove singularities and negative thermal expansion in highly oriented pyrolytic graphite with hexagonal Moiré superlattices. *Carbon Trends* **2021**, *3*, 100034. [CrossRef]

45. Taallah, A.; Odunmbaku, O.; Ivaturi, S.; Wen, J.; Liu, M.; Zhang, X.; Medranda, D.; Wang, S.; Boi, F.S. Water-assisted structural manipulation of ferromagnetically filled carbon onions: The case of high pressure Fe_3O_4. *Dae Solid State Phys. Symp.* **2019**, *2115*, 030119.

46. Claramunt, S.; Varea, A.; Lopez-Dıaz, D.; Velázquez, M.M.; Cornet, A.; Cirera, A. The Importance of Interbands on the Interpretation of the Raman Spectrum of Graphene Oxide. *J. Phys. Chem. C* **2015**, *119*, 10123–10129. [CrossRef]

47. Hesp, N.C.H.; Batlle-Porro, S.; Krishna Kumar, R.; Agarwal, H.; Ruiz, D.B.; Sheinfux, H.H.; Watanabe, K.; Taniguchi, T.; Stepanov, P.; Koppens, F.H. Cryogenic nano-imaging of second-order moiré superlattices. *Nat. Mater.* **2024**, 1–7. [CrossRef] [PubMed]

48. Sinner, A.; Pantaleón, P.A.; Guinea, F. Strain-induced quasi-1D channels in twisted moiré lattices. *Phys. Rev. Lett.* **2023**, *131*, 166402. [CrossRef]

49. Wang, P.; Yu, G.; Kwan, Y.H.; Jia, Y.; Lei, S.; Klemenz, S.; Cevallos, F.A.; Singha, R.; Devakul, T.; Watanabe, K.; et al. One-dimensional Luttinger liquids in a two-dimensional moiré lattice. *Nature* **2022**, *605*, 57–62. [CrossRef]

50. Trugenberger, C.A. Room-Temperature Superconductivity in 1D. Condens. *Matter* **2024**, *9*, 34.

51. Kopelevich, Y.; Torres, J.; da Silva, R.; Oliveira, F.; Diamantini, M.C.; Trugenberger, C.; Vinokur, V. Global room-temperature superconducivitity in graphite. *Adv. Quantum Technol.* **2023**, *1*, 2300230.